

On the vortical characteristics and cold-to-hot transfer of rarefied gas flow in a lid driven isosceles orthogonal triangular cavity with isothermal walls

Ehsan Roohi^{a,*}, Vahid Shahabi^a, Amir Bagherzadeh^b

^a High Performance Computing (HPC) Laboratory, Department of Mechanical Engineering, Ferdowsi University of Mashhad, 91775-1111 Mashhad, Iran

^b Isfahan University of Technology, Department of Mechanical Engineering, Isfahan, Iran

ARTICLE INFO

Keywords:

Triangular nano-cavity
Anti-fourier heat transfer
Shear stress gradient
Vortical behavior
Rarefied gas flow
DSMC

ABSTRACT

Rarefied gas flows in nano-scale isosceles triangular cavities with a motion away from the square corner are considered over a wide range of flow rarefactions regimes, i.e., $0.01 \leq Kn \leq 10$, using the direct simulation Monte Carlo (DSMC) method. We put emphasis to the rarefaction effects on the vortical behaviors and heat transfer patterns of rarefied monatomic and diatomic gases. We show that the primary vortices appearing in the triangular cavity are Moffat-type vortices, which disappear as velocity slip increases over the walls. However, an additional vortex is observed at $Kn > 1$ on the inclined wall attributable to the balance of the thermally driven flows from the cold to the hot region and flow induced by the primary vortex. We also report variations in the effective length scale of the fluid circulation with the Knudsen number. Our investigations specify that the competition between the Fourier term and shear stress gradient component of the heat flux constitutive relation results in the cold-to-hot transfer in triangular cavities. Also, heat flux patterns predicted by the asymptotic theory of the Boltzmann equation for the weakly non-linear flow and by the linearized form of the Regularized 13 moments (R13) equations are compared with the DSMC solution suitably at low Knudsen number regimes.

1. Introduction

Due to rapid progress in the fabrication of Micro/nano-electro-mechanical systems (MEMS/NEMS), a broad understanding of fluid mechanics and heat transfer mechanisms in these devices is required. MEMS/NEMS usually operate in a wide range of gas flow rarefaction including continuum, slip, transition, and free molecular regimes. The main criterion to determine the degree of departure from equilibrium condition in the flow field is the Knudsen number, i.e., the ratio of the molecular mean free path (λ) to a representative physical length scale of the geometry conducting the fluid, i.e., $Kn = \lambda/L$. As the very first deviations from the equilibrium distribution functions appear, the classical Navier-Stokes-Fourier (NSF) equations can be considered as the governing equations to treat the flow field [1]. The NSF equations together with appropriate velocity slip and temperature jump boundary conditions could be extended to the slip regime.

More realistic and accurate approaches are demanded to study rarefied flows where distribution functions noticeably depart from the equilibrium condition. In this regard, alternative governing equations can be derived from the Boltzmann equation with a higher order of approximation to investigate the non-equilibrium flows at the beginning of the transition regime [2]. On the other hand, direct simulation

Monte Carlo (DSMC) is another approach widely employed to solve the Boltzmann equation stochastically in the whole range of rarefaction regimes [3]. In DSMC, the gas is simulated as a set of moving particles which experience binary collisions as a means to update their velocities. DSMC is shown to be one of the most successful particle approaches, and it has been broadly utilized to model gaseous flows exposed to the non-equilibrium condition.

During the recent years, there was a broad set of scientific reports considering micro/nano flows using the DSMC technique. For example, Sebastião and Santos [4] performed a numerical investigation of a supersonic flow in a microchannel considering the effects of incomplete surface accommodation on the surface properties of the microchannel. Zhou et al. [5] simulated effects of a gas-surface interaction model in the DSMC technique on main gas properties in a circular microchannel. Akhlaghi et al. [6] presented an iterative technique (IT) for implementing wall heat flux boundary condition in the DSMC method that was accurate for both of cooling and heating wall heat flux. In a recent study [7], they introduced a modified iterative technique (MIT) for imposing a specific wall heat flux in the DSMC method. Moghadam et al. [8] investigated hydrothermal behavior and heat transfer characteristics in a thermal cavity and showed that heat flux variation decreased with increasing the Knudsen number. A review of DSMC

* Corresponding author.

E-mail address: e.roohi@ferdowsi.um.ac.ir (E. Roohi).

capability in predicting rarefied flow field in various micro/nano-systems is reported in Ref. [9].

Among different geometries considered in MEMS/NEMS, the lid-driven cavity flow is a simple geometry that could be observed in various industrial applications [10]. The vortical gaseous flow in quadrilateral lid-driven cavities has already been investigated at different rarefaction degrees by several authors [11–18]. John et al. [15] utilized the DSMC scheme for rarefied gas flow in a lid-driven cavity to show the existence of heat transfer from the cold to the hot region in the transition regime. However, no reason for this unusual behavior is reported. In another attempt, John et al. [16] studied the effect of incomplete surface accommodation on the heat transfer mechanisms in the lid-driven cavity. Mohammadzadeh et al. [17,18] employed the DSMC method to study heat flux and entropy behavior in micro/nanocavities.

Unique features such as cold to hot heat transfer are remarkable phenomena occurs in micro/nano-devices under rarefied condition. Rana et al. [19] studied the influence of rarefaction effects on the heat transfer in a thermal cavity using NSF equations with jump and slip boundary conditions and the regularized 13 moments (R13) equations. Vargas et al. [20] studied the thermally induced rarefied flow in a rectangular cavity with non-isothermal walls based on the numerical solution of the Shakhov kinetic equation and the DSMC method. Huang et al. [21] presented a unified scheme based on the kinetic model. They compared their results for lid driven cavity with those obtained by NSF solver and DSMC method and showed that the presented model has a superior capability than the NSF solver in capturing non-equilibrium rarefied flow such as cold-to-hot transfer.

Despite the extensive works focused on quadrilateral cavities, there have been a few reports on the triangular cavity flow, and all of them have been conducted in the continuum flow regime. According to [22], the most exciting feature of the low-Reynolds, continuum flow in triangular cavities is the occurrence of an infinite sequence of Moffat eddies of decreasing size and rapidly decreasing intensity towards the stationary corner [23,24]. Jagannathan et al. [25] used a spectral collocation method to compute the characteristics of incompressible, viscous flow in a lid-driven right triangular cavity for Reynolds numbers 100, 500 and 1000. Erturk et al. [26] simulated 2-D steady incompressible flows inside a triangular cavity and presented highly accurate numerical solutions. Gonzalez et al. [27] and Ahmed, and Kuhlmann [28] investigated the linear instability of the incompressible flow in the lid-driven triangular cavities using both theoretical and experimental approaches and showed that vortex behavior depends on the direction of the lid motion. A numerical analysis has been performed by Rahman et al. [29] to simulate double diffusive natural convection inside a triangular enclosure with the corrugated bottom wall using finite element method.

In the current study, we utilize the DSMC method to investigate the hydrodynamic and thermal characteristics of monatomic and diatomic flows in a triangular cavity in non-equilibrium regimes. According to our literature survey, there are no previous reports on flow and thermal field behavior in nano-scale triangular geometries. We report a definite change in vortex characteristics with the increased fluid rarefactions, and we emphasize the role of the thermal creep effects on the formation of a small vortex over the inclined surface of the cavity. Furthermore, we investigate the presence of cold-to-hot heat transfer in the transition and slip regimes. We compare our heat flux patterns with those of the asymptotic theory of the Boltzmann equation for the weakly non-linear flow (Sone's equation) [30] and a linearized form of the regularized 13 (R13) moments [31]. As our literature survey indicates, none of the features mentioned above have been considered in the previous investigations.

2. DSMC method and numerical setting

The DSMC method, developed by Bird [3], is a stochastic procedure

for solving the Boltzmann equation. The method is widely employed for treating rarefied gaseous flows either in hypersonic regime or at the micro and nano scales. In the DSMC algorithm, a finite set of simulator particles is utilized representing a significant number of real gas molecules. To improve numerical efficiency, DSMC splits the free flow movement and collision of simulated particles in each time step into two continuous processes. To satisfy this condition, simulation time step must be considered as a fraction of the mean collision time. In the free molecular movement, there is no interaction between the simulator particles. If a simulator hits the boundary, its state changes according to the boundary condition, e.g., it is reflected. New particles are created according to the inflow conditions. The second fragment of the particle evolution considers the collision term, where simulators collide changing their velocities. Various collision models such as no-time-counter (NTC) [4] and simplified Bernoulli Trials [32–37] has been developed in the framework of the DSMC method. A comprehensive review of DSMC collision models is reported in Ref. [38]. In this study, a modified version of the dsmcFoam [39–41] was used as our DSMC solver.¹ In the DSMC algorithm, the flow field is divided into computational cells representing geometrical boundaries and volumes needed for the sampling of the macroscopic properties. Also, the particles inside the same cell (or subcell) are permitted to collide. Variable hard sphere (VHS) and Larsen-Borgnakke Variable Hard Sphere (LB-VHS) collision models are used to model binary molecular interactions for monatomic and diatomic gases, respectively. Collision pairs are chosen based on the NTC method, in which the computational cost is proportional to the number of simulator particles [3,38]. In brief, the main steps in the DSMC method consist of initialization, moving the particles, indexing the simulators in new cells, performing collision between particles, and sampling the simulators within a cell to determine the macroscopic properties. We use the diffuse reflection model to treat all solid walls. Monatomic argon with a molecular mass of $m = 6.63 \times 10^{-26}$ kg, diameter of $d = 4.17 \times 10^{-10}$ m, and viscosity-temperature index of $\omega = 0.81$, and diatomic nitrogen with molecular mass and diameter of $m = 4.65 \times 10^{-26}$ kg and $d = 4.17 \times 10^{-10}$ m, and viscosity-temperature index of $\omega = 0.74$, respectively are simulated. The reference temperature was considered as $T_{\text{ref}} = 273$ K for both gas [3].

3. Flow configuration, grid & particle independent study

The schematic of the geometry of the nano-scale isosceles triangular cavity is depicted in Fig. 1. Three corners of the cavity are designated by A, B, and C. dashed lines denoted by DE and FG are vertical and horizontal centerlines, respectively. All walls' temperature is held at a constant temperature equal to the initial gas temperature inside the cavity, i.e., $T_{\text{wall}} = T_0 = 300$ K. The length of the horizontal and vertical walls of the isosceles triangle is considered $L = 100$ nm. The bottom driven-lid has a velocity of $U_{\text{wall}} = 100$ m/s in the positive x-direction. The reason of selecting the bottom wall as the driven wall is discussed in Appendix B at the end of the paper. The key parameter in rarefied flow, Knudsen number, is defined as the ratio of the mean free path to a characteristic length. Following [42], the latter is chosen as the effective height of the triangle, i.e., the ratio of the area to the side length of the triangle, i.e., $L/2$.

Unstructured isosceles triangular cells are utilized to divide the computational domains into small regions. The cell dimensions should be selected to be smaller than the gas mean free path [43–45]. Fig. 2-a shows the grid study test for velocity and density on the driven lid using three cell sizes, i.e., cell length equal to $\lambda/3$, $\lambda/4$, and $\lambda/6$, in which density is non-dimensionalized using the initial reference density. The figure shows that there is no considerable difference between the results obtained for $\lambda/4$ and $\lambda/6$ size grids; therefore, the grid consisting of cell

¹ This updated version is available with OpenFoam 2.4 for download in: <https://github.com/MicroNanoFlows/OpenFOAM-2.4.0-MNF>.

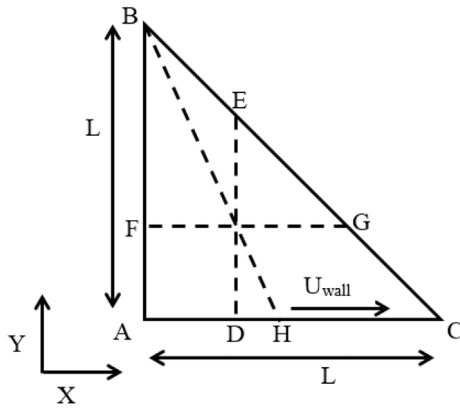


Fig. 1. The geometrical configuration of the micro/nano-cavity and lines over which flow properties are sampled.

triangular cavity with isothermal walls at specified Knudsen numbers/wall velocity.

4. Results and discussion

4.1. Circulation and velocity profiles

To investigate the non-equilibrium effects on the vortex strength in the nanocavity, the circulation of the velocity field, Γ , is considered. If \mathbf{V} is the fluid velocity and $d\mathbf{s}$ is a vector responding the differential length of the small element, the circulation around a closed surface is defined as:

$$\Gamma = \oint \mathbf{V} \cdot d\mathbf{s} = \int \text{rot}_n \mathbf{V} \cdot d\mathbf{A} = \sum_{i,j} \left[\frac{(V_{yi+1} - V_{yi,j})}{\Delta x} - \frac{(V_{xi+1} - V_{xi,j})}{\Delta y} \right] \Delta x \Delta y \quad (1)$$

where $\text{rot}_n \mathbf{V}$ stands for the curl of the velocity vector. For a square

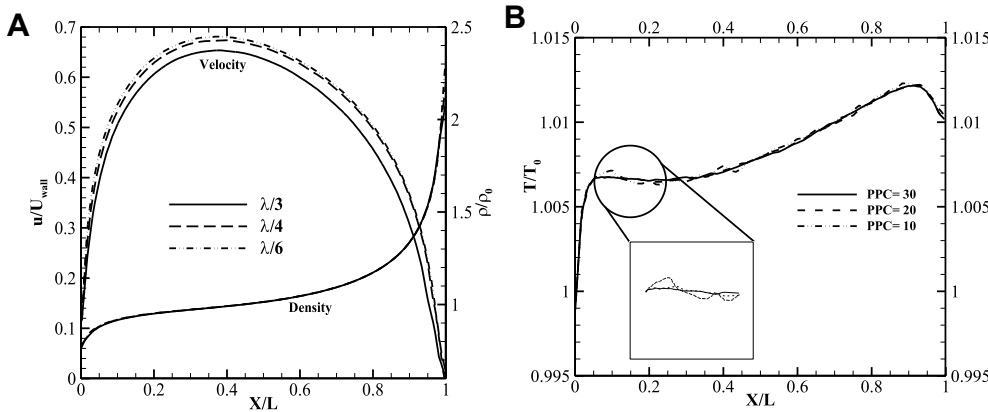


Fig. 2. a. Grid independence test results: normalized velocity and density distribution on the cavity moving wall; $Kn = 0.1$, $U_{wall} = 100$ m/s. b. Particle independence test results, distribution of normalized temperature on the cavity moving wall; $Kn = 0.1$, $U_{wall} = 100$ m/s.

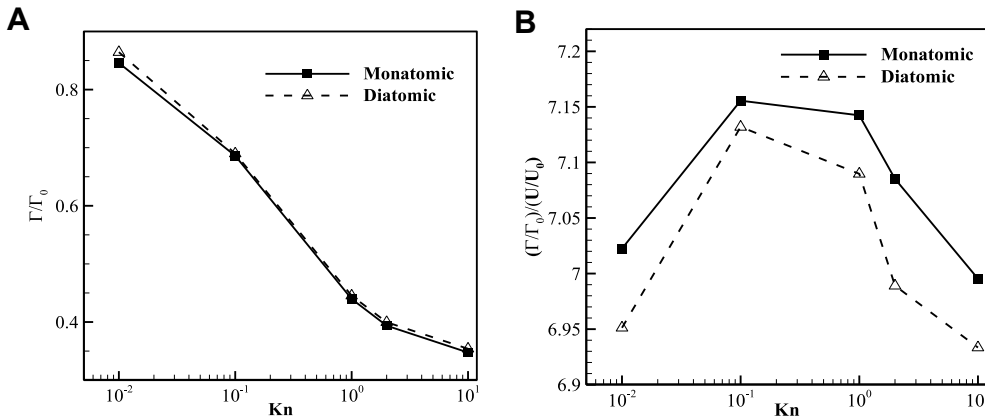


Fig. 3. a. Circulation of the mean velocity vector. b. The ratio of the normalized circulation to the normalized velocity.

size of $\lambda/4$ is selected for the rest of this study. The time step is chosen so that no molecule can cross more than one cell within one time-step, i.e., smaller than $1/3$ of the minimum of the mean collision time and mean transit time [18]. The effect of the number of particles per cell (PPC) on the accuracy of the temperature distribution (temperature jump) on the driven lid has also been investigated, as shown in Fig. 2-b. According to this figure, there is no change in the temperature profile as PPC increases from 20 to 30. Therefore, the number of simulated particles are considered to be 20 particles per each cell. This is a typical magnitude required by the NTC collision technique [46]. The sampling of results started as soon as the flow arrives at the steady state conditions. Simulation well continued after this time to suppress statistical scatters in the DSMC results. It should be mentioned that presented results in the following sections are valid for an isosceles orthogonal

element (cell), the surface area element, dA , is defined as $\Delta x \times \Delta y$, where Δx and Δy are cell length and height. i, j are two indices spanning all cells in the axial and normal directions, therefore, the summation is taken over the entire computational cells of the cavity. Fig. 3-a shows the flow circulation, normalized with $\Gamma_0 = U_{wall} \times L$, in a variety of Knudsen numbers. It is observed that for the both monoatomic and diatomic flows, growing non-equilibrium effects gradually damps the induced driving momentum of the moving lid, and as a result, diminishes the strength of the vortex in the cavity. The main reason for this behavior is the decrease of the Reynolds number with the increase of the flow rarefaction, i.e., $Re \sim 1/Kn$; i.e., increased viscous effects subsequently decreases the velocity gradient and flow tendency to circulate. From a molecular point of view, higher rate of intermolecular collision helps the vortex organization and formation while at higher

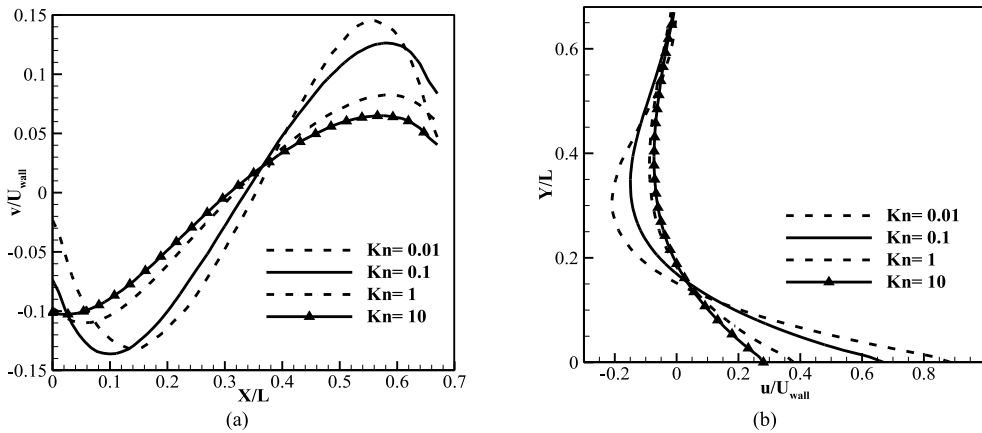


Fig. 4. Comparison of non-dimensional velocity profiles for argon flow along, a) the horizontal centerline of the cavity, patch FG, and b) the vertical centerline of the cavity, patch DE.

rarefied conditions contribution of molecule-molecule collisions decreases and wall contribution enhances which is more diffusive. The ratio of circulation to the average velocity in the domain is shown in Fig. 3-b. As argon mass is heavier than nitrogen, the average velocity of argon is smaller. It is because argon gains relatively smaller velocity upon reflecting from the walls as the reflected molecular velocity is proportional with $(T_w/m)^{1/2}$. This parameter (Γ/U) shows a characteristic length over which the circulation in the cavity takes effect. The figure indicates that this length is higher for monatomic gas and reaches to the maximum level at about $Kn = 0.1$ for both gases.

Fig. 4 shows the vertical and horizontal components of velocity vectors along the horizontal and vertical centerlines of the cavity over a wide range of Knudsen numbers, i.e., $0.01 \leq Kn \leq 10$ and $0.043 \leq Re \leq 43$ for argon gas flows. This figure shows a reduced curvature of the horizontal velocity in the higher Knudsen number conditions, which can be attributed to the reduced vortex strength in the nanocavity at high rarefaction regimes, i.e., lower driving force. Similar to [47], our simulation illustrated almost the same velocity profile along centerlines of the geometry for the nitrogen gas. Therefore, it is not depicted here.

4.2. Center of vortex location and velocity slip

The variation of the location of the center of the vortex in the cavity with the Knudsen numbers is plotted in Fig. 5-a. With the increase of the Knudsen numbers, the viscous dissipations in the flow field augment. In other words, the induced kinetic energy from the bottom lid dissipates rapidly as the flow rarefies more. This is another interpretation of the higher slip between the wall velocity and gas layer velocity adjacent to the wall at higher rarefaction regimes.

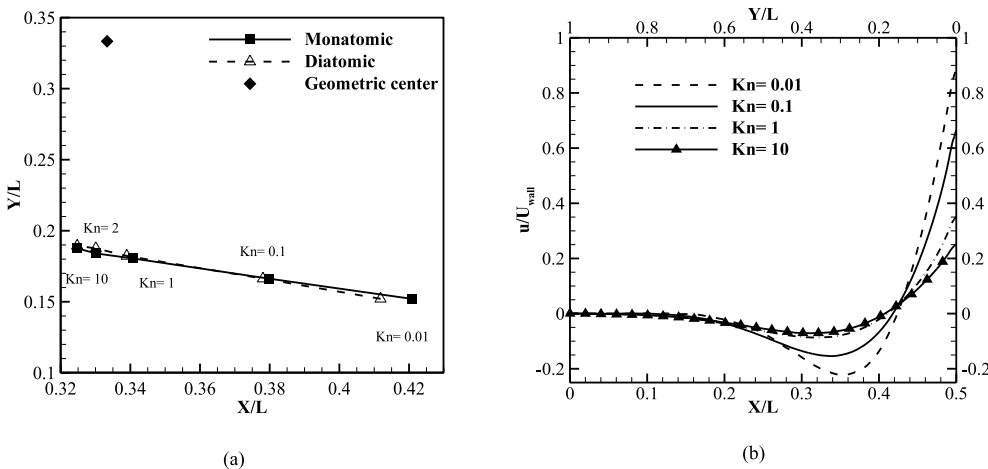


Fig. 5. (a) Variation of the center of the vortex location with the Knudsen, (b) u velocity along the patch BH for nitrogen gas flow.

Consequently, the pushing force on the gas reduces which results in a shift of the center of vortex toward the left. As Knudsen number increases further, i.e., $Kn > 2$, the center of vortex moves away from the geometric center of the cavity. In general, it is observed that with increasing the Knudsen number, the center of vortex moves from the driven lid toward the left top corner of the cavity. This observation is in agreement with Ref [48]. To elaborate on the effects of Knudsen number on the strength of the vortex, the variation of x-velocity along the patch connecting the top corner to the bottom lid (patch BH) is demonstrated in Fig. 5-b. The figure shows that normalized velocity changes by 20% at $(X/L, Y/L) = (0.35, 0.30)$ at the lowest investigated Knudsen number. The induced velocity over the line reduces as the flow rarefies more.

Frames in Fig. 6 show slip velocity over three walls of the cavity. The first frame indicates a higher slip at higher Knudsen numbers, i.e., at $Kn = 10$, fluid velocity falls to less than 30% of the moving lid velocity. However, the fluid behavior on the vertical wall, frame (b) is different. Just at the vertical corner, the fluid velocity is affected by the fluid slip adjacent the moving lid, but the fluid velocity falls farther along the wall, and this decrease is faster at lower Knudsen numbers. This is due to lower velocity slip at lower rarefaction conditions. However, the fluid velocity on the inclined wall is affected by both of velocity slip and induced flow by the main vortex of the cavity on this wall. The stronger vortex occur at $Kn = 0.01$; therefore, the maximum velocity is observed slightly farther from the corner in this condition, but the fluid velocity rapidly falls as the fluid moves further along the inclined wall. On the other hand, the induced velocity at $Kn = 0.1$ is larger than the next two cases for $0.0 < Y/L < 0.5$. This is because of the larger effective length of the vortex in this condition, see Fig. 3-b.

Shown in Fig. 7 are the velocity streamline plotted over velocity

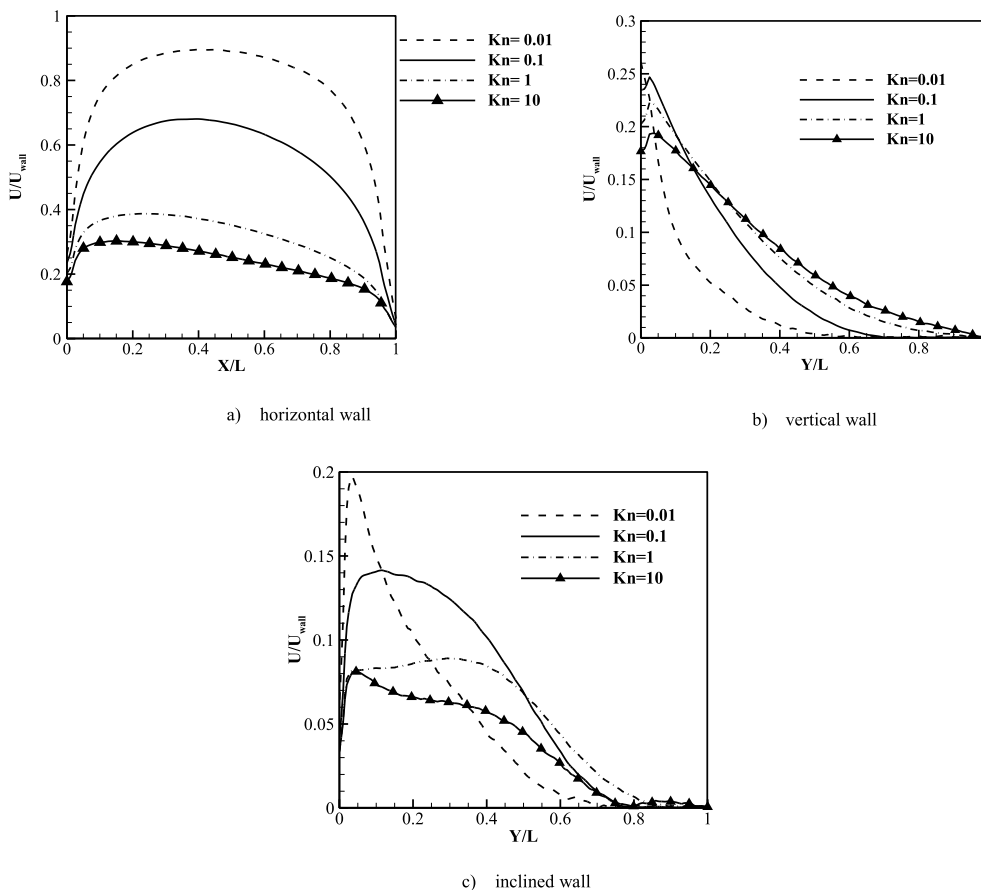


Fig. 6. Normalized velocity slip magnitude over the walls of the triangle.

contours for the nitrogen gas flow at various Knudsen numbers from $Kn = 0.01$ to $Kn = 10$. At the two lowest Knudsen numbers, there are a series of vortices inside the cavity, which is in keeping with Moffat's observation for low Reynolds number flow near sharp corners [24,25]. The primary vortex created due to the bottom wall motion is quite stronger compared to other vortices, and its size increases as the fluid Knudsen number increases to $Kn = 1$. Zones of stagnant fluid form on the right corners as the primary vortex separates from the bottom wall. In addition to the main vortex in the cavity, there are a few small vortices near the top corner, which disappear as Kn increases in the transition regime, i.e., $Kn = 1$. This phenomenon could be associated with the fact that by increasing the Knudsen number the intermolecular interaction decreases and molecule-surface interaction increases, once a particle collides with the bottom lid it moves to the top corner with higher energy level, consequently resulting in removing the small vortices.

Moreover, increased slip velocity on the vertical wall could be another reason for the vortices disappearance, see Fig. 6-b. At $Kn = 2$, a small vortex appears adjacent to the inclined wall, which grows as Knudsen number increases. It should be noted that this eddy, attached to the inclined wall, is entirely different in character from the corner eddies. The appearance of this vortex could be attributed to the balance of thermal creep flow, moving the fluid from the top cold corner toward the bottom hot corner, and the induced flow by the primary cavity vortex. This phenomenon happens not only for the nitrogen gas flow but also for the argon gas flow.

It should be noted that thermal creep flow is not a question of whether there is a temperature gradient in the wall, but it is a question of the temperature gradient in the gas adjacent to the wall. To describe thermal creep flow, we assume there is a temperature gradient in the

gas adjacent to the wall, with higher temperatures at larger x . We consider particles that are one mean free path away from the wall and flying towards the wall. If we consider now a location x at the wall, the particles that hit the wall come either from $x-dx$ or $x+dx$. Particles coming from $-dx$, where the temperature is lower, will have in average a smaller velocity than those that come from $+dx$. In collisions with the wall at x , both types of particle transfer tangential momentum to the wall. Note that particles leave the diffuse walls in a Maxwellian state, hence their average tangential momentum when leaving the wall is zero. The momentum transferred to the wall moves towards the $-x$ direction since the “hotter” particles fly in that direction. The gas transfers momentum to the wall; the wall moves towards the cold. Or, changing the observer frame, when the wall is fixed, and there is a temperature gradient adjacent to the wall, the gas will move towards the warm region according to Newton's third law. In our case, a suitable temperature gradient (temperature change per length) is created adjacent the hypotenuse, see Fig. 12. As Kn increases, thermal creep force enhances resulting in a net flow from cold to hot region.

4.3. Shear stress profile

Fig. 8 illustrates the normalized shear stress profile, non-dimensionalized by $\tau_0 = 0.5\rho_\infty U_{wall}^2$, along the horizontal centerline and lid driven of the cavity, where ρ_∞ is the initial density at the corresponding Knudsen number. From the molecular point of view, normalized shear stress τ_{xy} is proportional to $\langle c_x c_y \rangle$, where c_x and c_y are peculiar velocities of the molecules and $\langle \rangle$ stands for averaged values. The $\langle c_x c_y \rangle$ term means the transport of x -momentum per unit mass by the vertical component of the velocity. As the molecule-molecule interactions and associated relaxation of molecular velocities decreases with

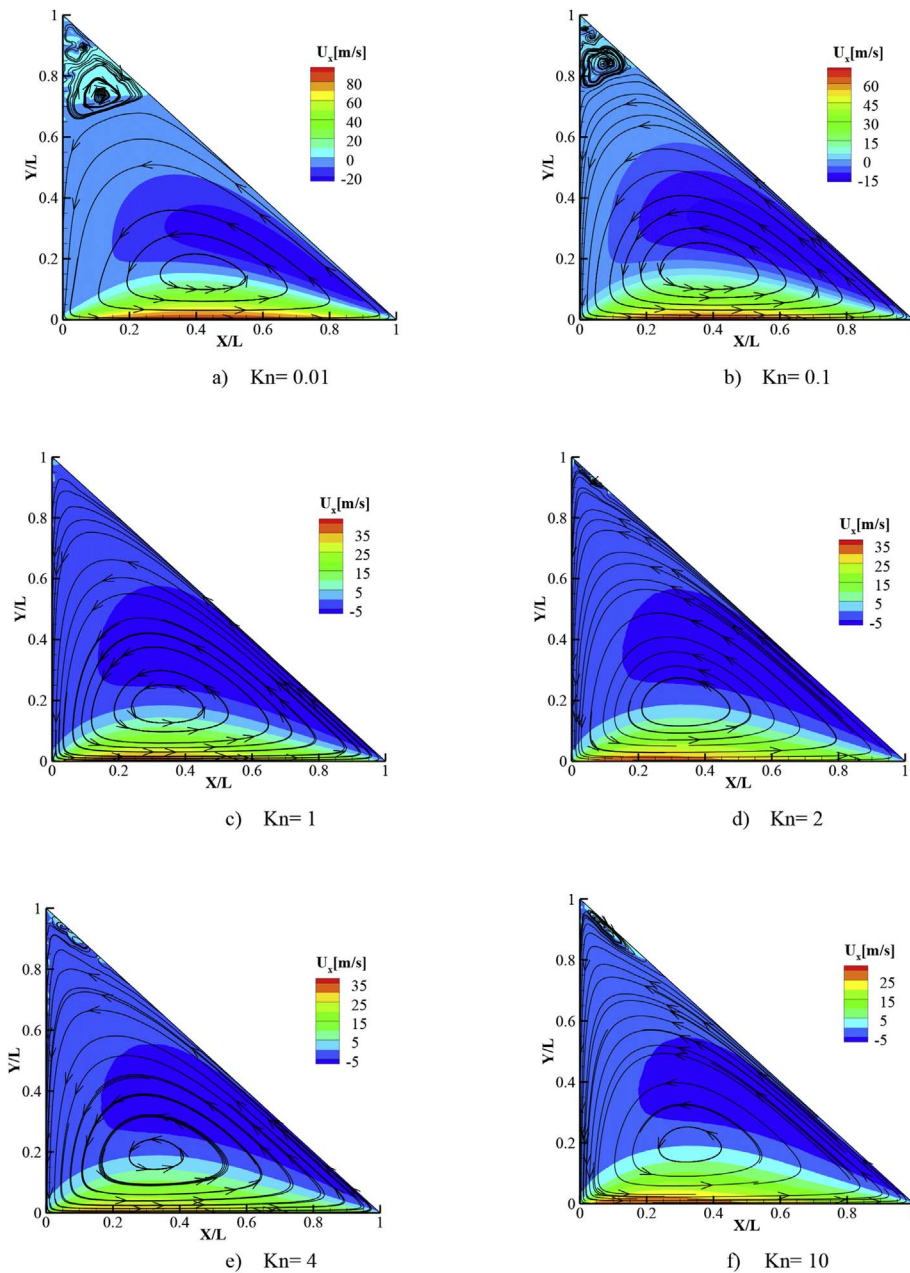


Fig. 7. Velocity streamlines overlaid on u-velocity contours for nitrogen gas flow at different Knudsen numbers.

an increase in the Knudsen number, a larger number of molecules come directly from the walls with less sharing of the gained x-momentum from the moving wall by other particles; as a result, the net amount of $\langle c_x c_y \rangle$ increases. However, if a dimensionalized shear stress was plotted, the magnitude becomes much smaller at more rarefied conditions due to reduced gas density, i.e., $\tau_{xy} = \rho \langle c_x c_y \rangle$. In the transition and free molecular regimes, the level of shear stress is higher in the right segment of the flow field as flow approaches the inclined wall and experiences geometrical contraction, while a symmetric distribution of normalized shear stress is observed at the early slip regime, $Kn = 0.01$. Obviously, Fig. 8 shows that the magnitude of non-dimensionalized shear stress for nitrogen remains larger than argon flow in all rarefaction regimes. The shear stress of nitrogen is higher than that of argon in a dimensionalized ground as well. This behavior could be justified by observation reported in Fig. 3-b, which showed that average fluid velocity is smaller for the argon case due to a higher mass of the argon;

and characteristic length is higher for argon, therefore, nitrogen gas experiences larger velocity gradients and hence larger shear stress.

4.4. Temperature profile

Frames in Fig. 9 shows the flow temperature along the horizontal centerline of the cavity at various rarefaction regimes for nitrogen and argon flows. Evidently, the temperature is higher on the right wall due to the formation of the stagnation point on the right corner of the triangle. On the other hand, fluid expansion near the left corner decreases the gas temperature. The more the flow deviates from equilibrium, the less frequently inter-molecular collision takes place; as a result, the gas molecules manage to conserve their gained energy from the driving lid. This justifies the higher (colder) temperature of the gas on the right (left) side at higher rarefaction conditions. The figures also reveal that as the flow passes the slip regime toward the transition one, the

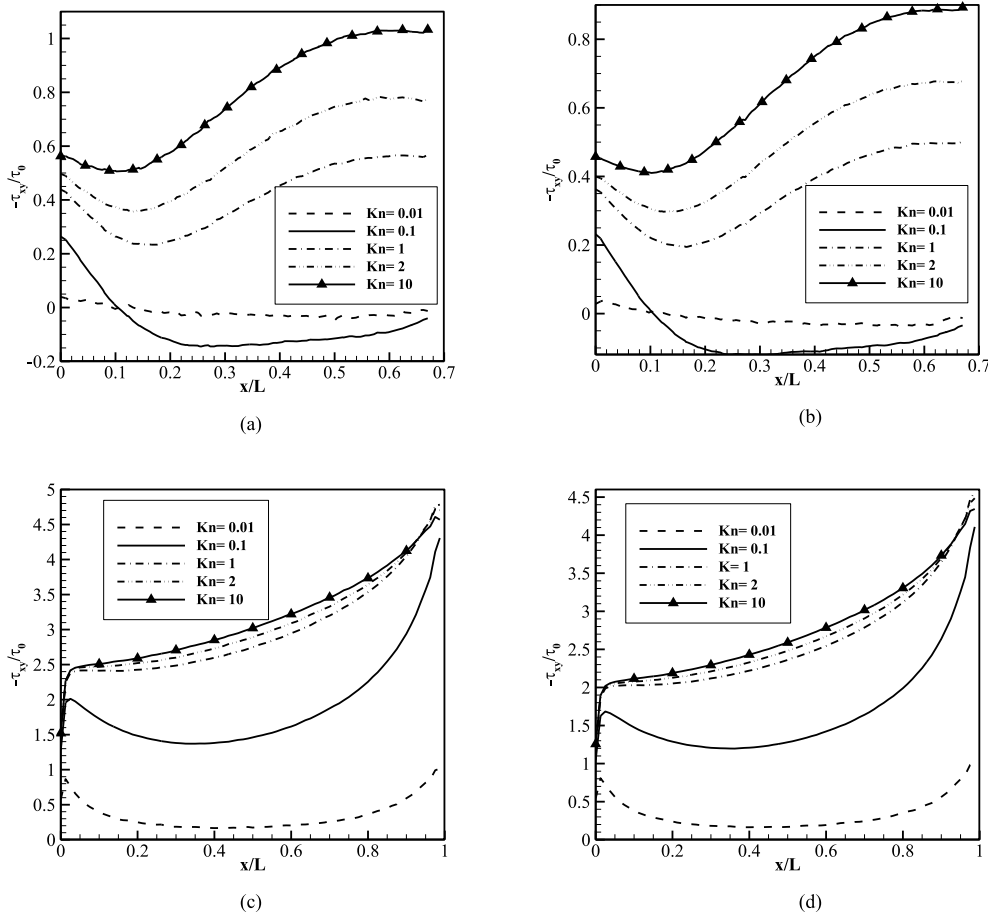


Fig. 8. Shear stress profile along the horizontal centerline and cavity lid: a, b) horizontal centerline diatomic nitrogen flow and monatomic argon flow respectively. c, d) cavity lid, nitrogen flow and monatomic argon flow respectively.

variations in temperature becomes more noticeable. This observation could also be attributed to the increased rate of intermolecular collisions at the slip regime, which lead the gas temperature toward a more uniform distribution.

Furthermore, there is a difference between argon and nitrogen temperature profiles indicating higher temperatures for monatomic gas in all rarefaction regimes. The lower temperature for the nitrogen flow could be attributed to the fact that diatomic molecules have both translational and rotational modes of energy, i.e., a higher degree of freedom; therefore, the same level of transferred kinetic energy from the moving lid increases the nitrogen temperature less.

Variations of temperature jump along the driven lid are plotted in Fig. 10 for both gases. Reduced binary collision due to rapid motion of the bottom wall leads to a significant departure from the equilibrium

state in the bottom left region at all rarefaction regimes. This results in a significant temperature jump at the vicinity of $X/L = 0$. However, the equilibration of the gas molecules at lower Knudsen numbers reduces this jump as flow moves along the wall, while the jump again increases as the flow approaches the other non-equilibrium spot, i.e., right corner stagnation point at $Kn = 0.01$. In general, temperature jump increases as the flow moves to the transition regime, while the reduced rate of collisions almost keeps the temperature jump gained at the left corner for the whole length of the wall. Decreased temperature jump of the nitrogen gas in comparison with the argon gas is in agreement with the analytical, moment-based temperature jump expression of Rahimi and Struchtrup [49] for polyatomic gases, which indicated that increasing the only internal degree of freedom will reduce the temperature jump.

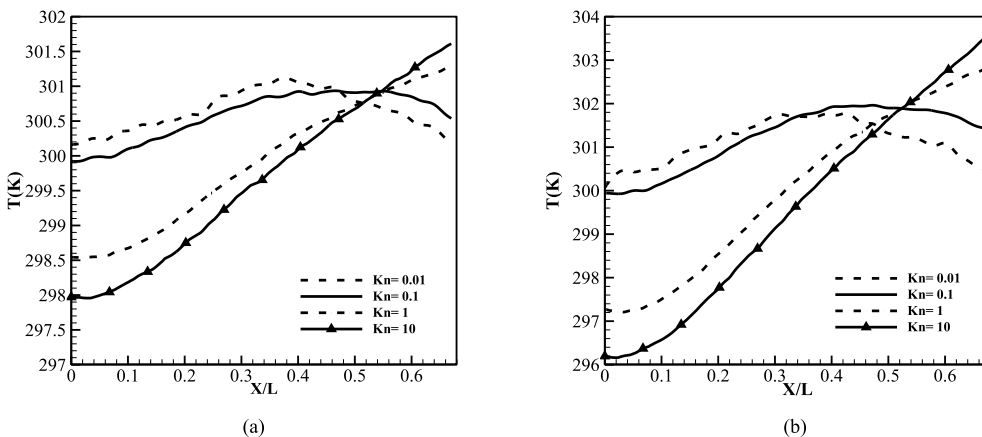


Fig. 9. Comparison of temperature profile along the horizontal centerline of the cavity: a) diatomic nitrogen flow and b) monatomic argon flow.

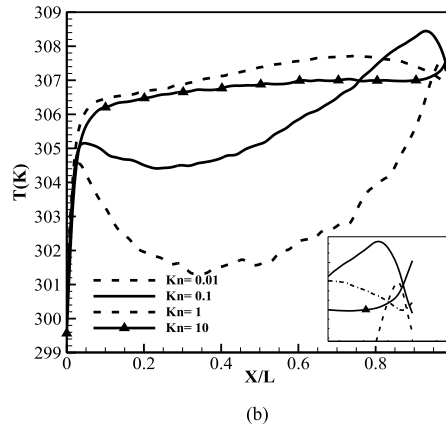
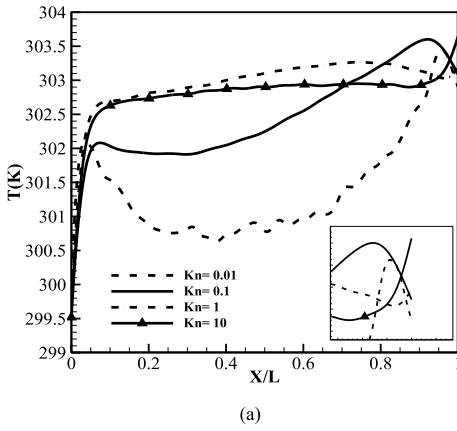


Fig. 10. Comparison of the rarefied flow temperature jump along the driven lid of the cavity: a) diatomic nitrogen flow and b) monatomic argon flow.

4.5. Cold to hot heat transfer

The continuum-based Fourier's law cannot analyze heat transfer phenomena in the rarefied gas flow regime [30,50]; therefore, more advanced constitutive laws should be considered to evaluate heat transfer characteristics at non-equilibrium conditions. Here, to compare with the DSMC solution, the asymptotic theory of the Boltzmann equation, derived by Sone [30], and a linearized form of the regularized 13 moments (R13) equations of rarefied gas dynamics [31] are taken into account to predict the heat flux pattern in the flow field. Sone constitutive relation for the heat flow vector is defined as follows:

$$Q = KQ_1 + K^2Q_2 + K^3Q_3 \quad (2)$$

$$Q_1 = 0 \quad (3)$$

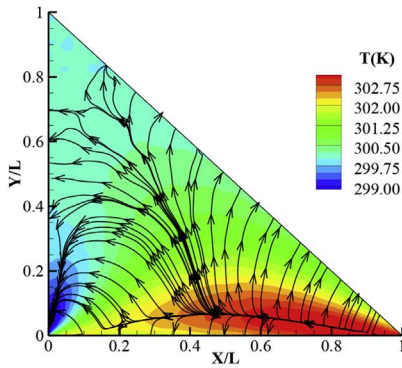
$$Q_2 = -\frac{5}{4}\gamma_2 \frac{\partial \tau^{**}}{\partial x_i} \quad (4)$$

$$Q_3 = -\frac{5}{4}\gamma_2 \frac{\partial \tau^{**}}{\partial x_i} - \frac{5}{4}\gamma_5 \tau^{**} \frac{\partial \tau^{**}}{\partial x_i} + \frac{1}{2}\gamma_3 \frac{\partial^2 u_i^{**}}{\partial x_j^2} \quad (5)$$

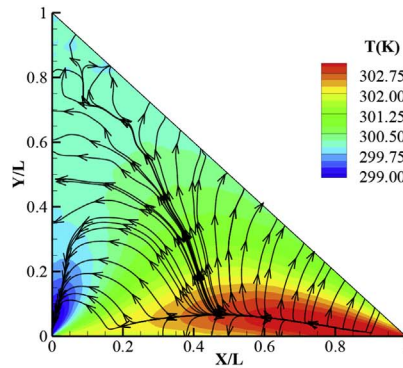
Where:

$$K = Kn \frac{\sqrt{\pi}}{2} \quad (6)$$

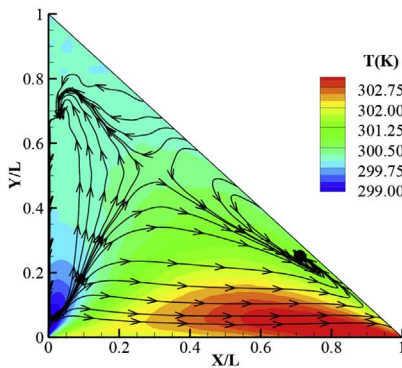
$$\tau^{**} = \frac{T - T_0}{T_0}, u_i^{**} = \frac{u_i}{\sqrt{2RT}}, x_i = \frac{X_i}{L} \quad (7)$$



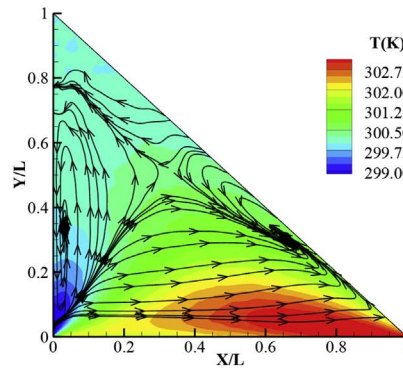
a) Heat lines of $-\frac{5}{4}\gamma_2 \frac{\partial \tau^{**}}{\partial x_i}$ term



b) Heat lines of $\frac{5}{4}\gamma_5 \tau^{**} \frac{\partial \tau^{**}}{\partial x_i}$ term



c) Heat lines of $\frac{1}{2}\gamma_3 \frac{\partial^2 u_i^{**}}{\partial x_j^2}$ term



d) Heat lines predicted by Eq. (2)

Fig. 11. Heat lines of different terms from the Sone's constitutive law drawn over temperature contour, $Kn = 0.1$.

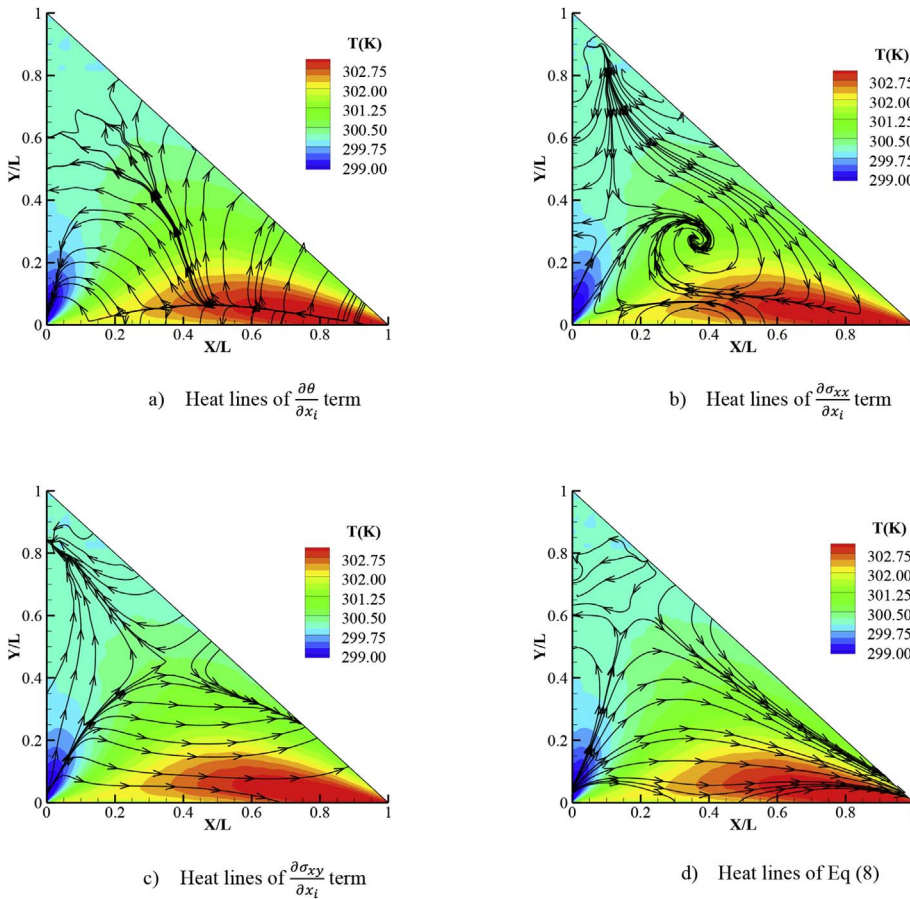


Fig. 12. Heat lines from the components of the R13 equation, $Kn = 0.1$.

Where superscript “**” refers to non-dimensional parameters, R and T_0 are gas constant and the initial gas temperature, respectively. The transport coefficients used in Eq. (5) are set as $\gamma_2 = 1.9222$, $\gamma_3 = 1.9479$ and $\gamma_5 = 0.9611$ [30]. The second term in Eq. (2) is the Fourier term while the last term in this equation consists of various terms including the second derivative of the velocity field. Therefore, according to the constitutive law of Ref. [30], heat flux could be a function of velocity field curvature at the rarefied condition. Fig. 11(a–c) and (d) show the heat lines computed from individual terms of Eq. (5), and the summations of contributions, respectively. As the figures demonstrate, the magnitude of $\frac{\partial^2 u_i^{**}}{\partial x_j^2}$ term is more influential than the other components of Q_3 . Therefore, the interaction between the Fourier term $-\frac{\partial \tau^{**}}{\partial x_i}$ in Q_2 and $\frac{\partial^2 u_i^{**}}{\partial x_j^2}$ in Q_3 determines the overall heat flux lines behavior. Moreover, the Figure shows that heat line concerned to $-\frac{\partial \tau^{**}}{\partial x_i}$ moves from the hot to cold region in the cavity; while the second derivative of the velocity $\frac{\partial^2 u_i^{**}}{\partial x_j^2}$ is responsible for to heat transfer from the cold region to the hot one.

Rana et al. [31] presented a linearized form of the heat flux constitutive law of the regularized 13 moments (R13) equations of rarefied gas dynamics as follows:

$$Q_i = -\frac{15}{4}\mu\frac{\partial\theta}{\partial x_i} + \frac{3}{2}\frac{\mu}{p}\theta\frac{\partial\sigma_{ik}}{\partial x_k} \quad (8)$$

Where:

$$\theta = \frac{T}{T_0}, x = \frac{x}{L}, \sigma_{ik} = \frac{\sigma_{ik}}{\rho_0 T_0} \quad (9)$$

σ_{ik} is the stress tensor and ρ_0 is the initial density at the corresponding Knudsen number. Our numerical results demonstrate that the $\frac{\partial\sigma_{xx}}{\partial x}$ and $\frac{\partial\sigma_{yy}}{\partial y}$ components are notably smaller than the other terms. Thus, the direction of heat flux depends on the interplay between the contributions of $-\frac{\partial\theta}{\partial x_i}$ and $\frac{3}{2}\frac{\mu}{p}\theta\frac{\partial\sigma_{ik}}{\partial x_k}$. Fig. 12 shows the heat lines from components of Eq. (8) and the summation of contributions. The $\frac{\partial\sigma_{xy}}{\partial x_i}$ term contribution shows a strong cold to hot transfer along the lid motion.

It should be noted that both of Sone equations and linearized R13 equation contain one term depending on temperature gradient (see Figs. 11-a and 12-a) and another term depending either on the second velocity gradient or shear stress tensor gradient. At small Kn , non-equilibrium shear stress mainly consists of velocity gradient, but these two are not necessarily the same, i.e., as local non-equilibrium enhances near the right corner of the cavity, Fig. 11-c (velocity gradient) and 12-c (shear stress gradient) show slight difference there. In overall, both terms shows a saddle point in the heat flux lines while the location of saddle point differs.

A comparison between Sone's, linearized R13 and DSMC prediction for the heat flux lines is depicted in Fig. 13. The figure shows heat lines plotted over the temperature contours at various Knudsen numbers. Compared to the DSMC solution, Sone's relation suitably predicts heat line patterns at lower Knudsen numbers, however; R13 solution shows an improved accuracy near the vertical wall at $Kn = 0.1$. Besides, the anti-Fourier, cold to hot heat transfer is visible in the cavity geometry in the vicinity of the bottom lid at lower Knudsen numbers. As the flow rarefies more to $Kn = 1$, the cold to the hot region occupies most of the geometry, i.e., heat lines do not originate from the left bottom corner but the left and bottom walls directed towards the inclined surface.

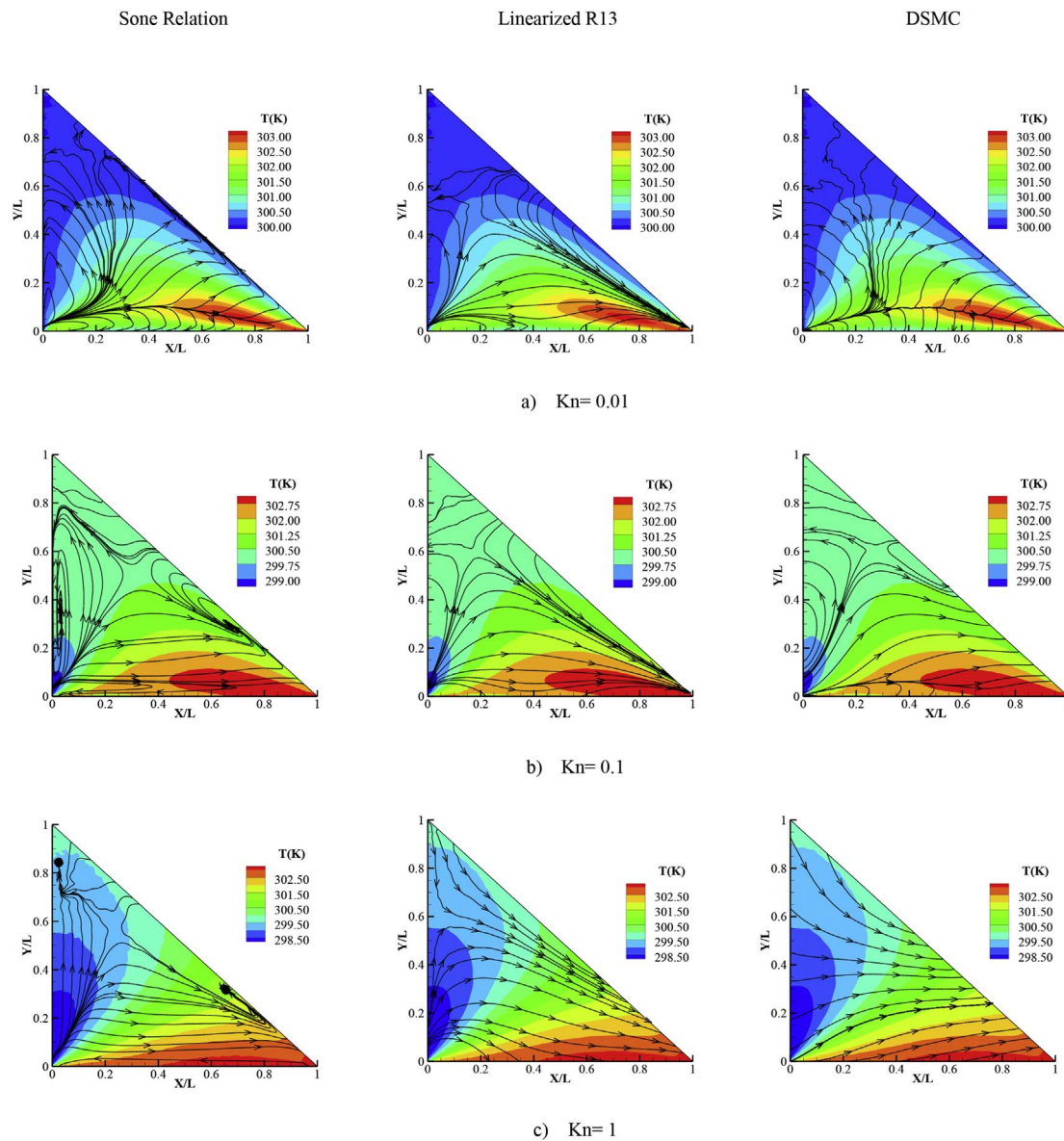


Fig. 13. Heat flux lines in the nano-scale lid driven triangular cavity from different solutions.

5. Concluding remarks

Rarefied gas flows inside the lid-driven nano-scale isosceles triangular cavities were investigated over a wide range of Knudsen numbers using the direct simulation Monte Carlo technique. The results show that vortical characteristics of the flow inside triangles are influenced not only by the geometrical configuration but also by the rarefaction effects. While the smallest members of the Moffat-family vortices disappear as the Knudsen number increases in the transition regime, another thermally-originated vortex appears in the top corner of the inclined wall at the mid-transition regime. For the geometry considered here, shear stress shows a distinct behavior at slip and transition regimes, i.e., a uniform distribution of shear on the cavity centerline at the slip flow regime transforms to a more focused shear on the inclined wall at the transition flow regime due to the geometrical constraint of the inclined surface. On the other hand, heat flux patterns inside the geometry show a strong cold-to-hot transfer near the moving lid at the

slip regime, which is attributed to strong bends in the velocity profile at the corners of the cavity, amplifying the velocity gradient contribution in the heat flux constitutive law (second order in Knudsen number) compared to the first order Fourier term. With the further increase of the Knudsen number in the transition regime, the regions of cold to hot transfer almost occupy most of the geometry while most of the heat lines is directed toward the inclined surface of the triangle.

Acknowledgements

The authors would like to acknowledge the financial support from the Ferdowsi University of Mashhad under Grant No. 40600. The authors also acknowledge Dr. Tobias Baier from the Institute for Nano- and Microfluidics, Technische Universität Darmstadt and Prof. Stefan Stefanov from Bulgarian Academy of Science, Sofia, Bulgaria for fruitful discussions regarding the results presented in this paper.

Appendix A. Fractional statistical errors in simulations

Hadjiconstantinou et al. [51] derived expressions for the magnitude of statistical errors due to thermal fluctuations in DSMC simulations. Based on Ref [51], the fractional statistical errors in DSMC results for density, velocity, and pressure are given by:

$$E_p = \frac{1}{\sqrt{MN_0}} \frac{1}{Ac}$$

$$E_u = \frac{1}{\sqrt{MN_0}} \frac{1}{ACMa\sqrt{\gamma}}$$

$$E_p = \frac{\frac{Ac\sqrt{\gamma}}{\sqrt{MN_0}} p_0^i}{p_0}$$

where M , N_0 , AC and Ma are number of independent statistical samples, number of particles in a sampling cell, the ratio of the fluid's sound speed to the speed of sound at the “reference” ideal gas at the same temperature, and the local Mach number, respectively. Also, $\gamma = C_p/C_v$ is the ratio of the specific heats and k is Boltzmann's constant. $p_0^i = N_0 k T_0 / V$ is the pressure of an ideal gas under the same conditions, V is the volume of the statistics cell and T_0 is the average temperature. For a typical run at $Kn = 0.1$, the statistical fractional errors are plotted and reported in Fig. A-1 considering number of samples of $M = 2.5 \times 10^6$. The figure shows that statistical scatters is quite low for all fluid parameters expect velocity. The maximum fractional error occurs for velocity on the top corner of the cavity as fluid Mach number is minimum there.

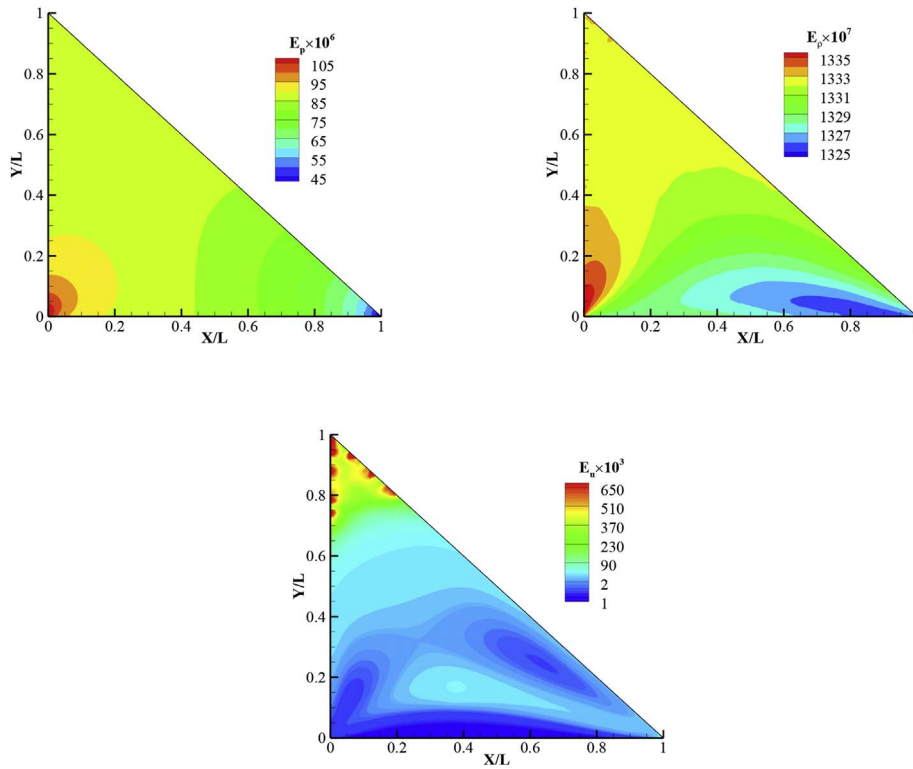


Fig. A-1. Fractional error in pressure, density, and velocity.

Appendix B. Hypotenuse wall movement

The effect of motion of hypotenuse wall of the cavity with a velocity magnitude of 100 m/s (U_x, U_y) = (80 m/s, 60 m/s) moving towards the bottom corner at various Knudsen numbers is shown in Fig. B-1. Nitrogen gas is considered. The figure shows that there is just one vortex in all rarefaction regimes. Fig. B-2 shows heat lines plotted over temperature contours. For all case, there is a heat flux from hot to the cold region. The low-temperature region increases as Kn increases. Both figures show that there are not any distinct behavior for hypotenuse motion. Also, the position of the center of the vortex slightly changes by Knudsen number increase, see Fig. B-3. As expected, center of the vortex position is closer to the right side of the of geometry. The normalized circulation magnitude depicted in Fig. B-3 is the same as the magnitude reported for bottom wall motion as the same velocity is considered in both cases. In overall, we did not focus on hypotenuse motions in this paper because the results for bottom wall motion seems more challenging with distinct changes in the vortical structure and possibility of cold to hot transfer.

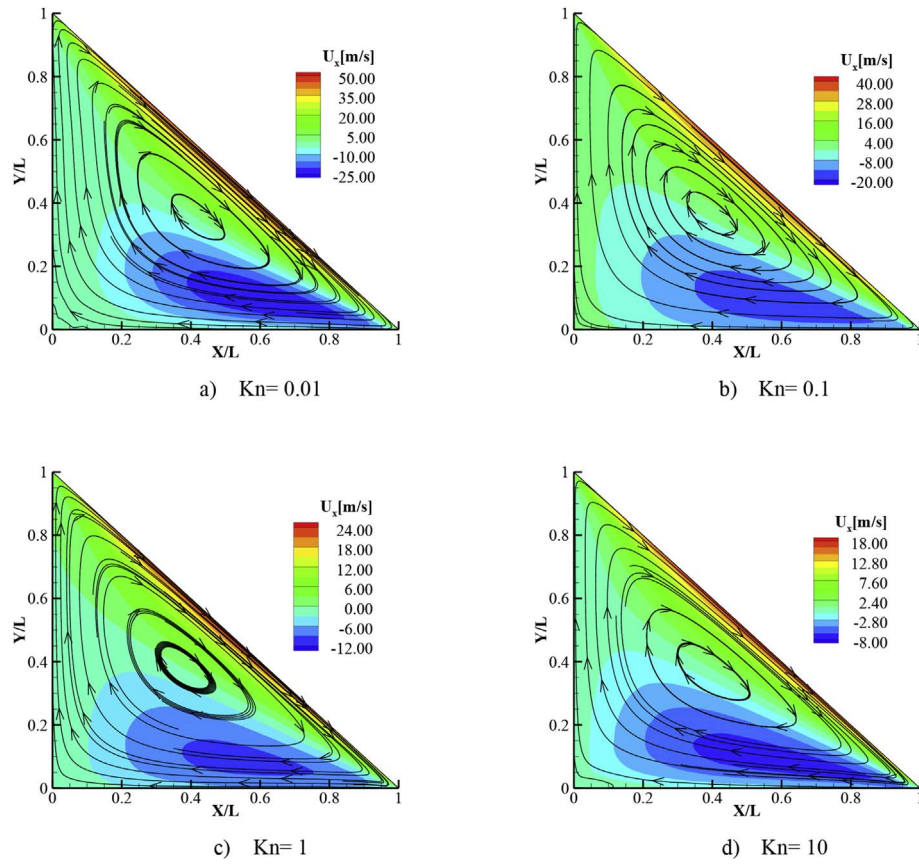


Fig. B-1. Velocity streamlines overlaid on u-velocity contours for nitrogen gas flow at different Knudsen numbers for the hypotenuse movement case.

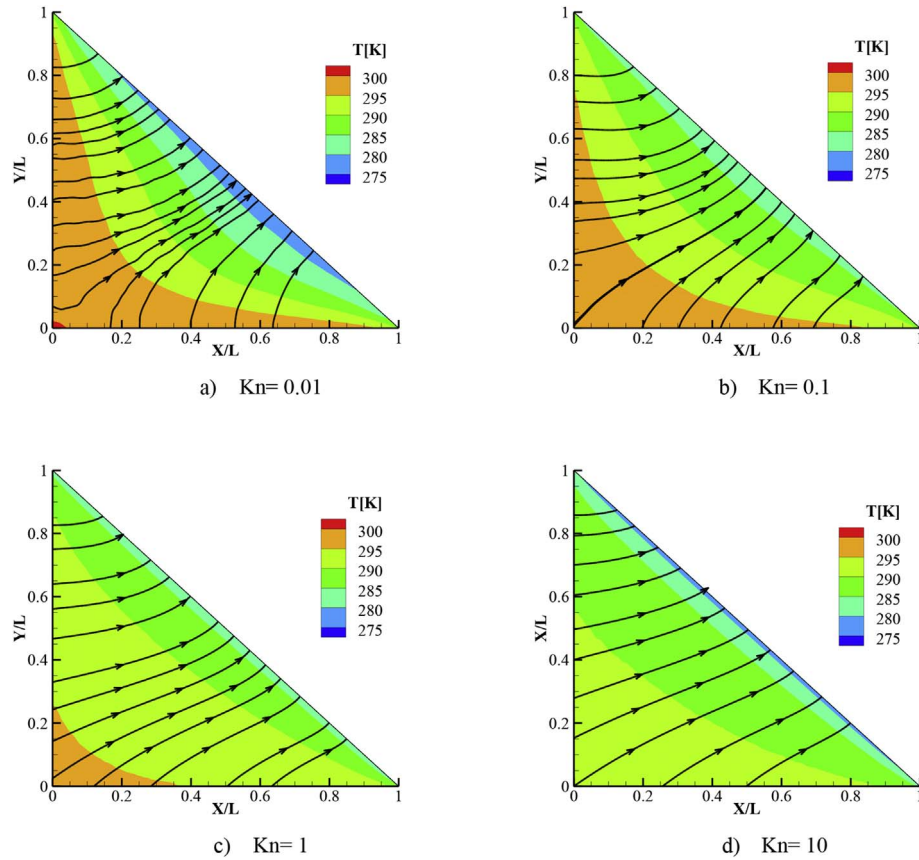


Fig. B-2. Heat lines overlaid on temperature contours for nitrogen gas flow at different Knudsen numbers.

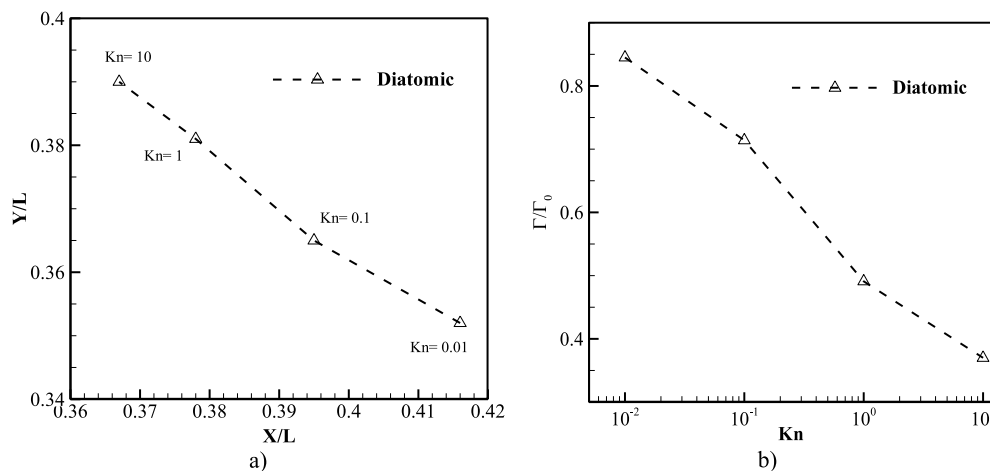


Fig. B-3. a) Center of vortex location, b) normalized circulation.

References

- [1] W.W. Liou, Y. Fang, *Microfluid mechanics: principles and modeling*, McGraw-Hill Education, New York, 2006.
- [2] F.B. Bao, J.Z. Lin, Continuum simulation of the microscale backward-facing step flow in a transition regime, *Numer Heat Transf Part A Appl* 59 (8) (2011) 616–632.
- [3] G.A. Bird, *Molecular gas dynamics and the direct simulation of gas flows*, Oxford University Press, 1994.
- [4] I.B. Sebastião, W.F. Santos, Gas–surface interaction impact on heat transfer and pressure distributions of a high speed microchannel flow, *Appl Therm Eng* 62 (1) (2014) 58–68.
- [5] H. Zhou, G. Cai, B. He, Effects of wall conditions on flow field in a circular micro-channel, *Appl Therm Eng* 109 (2016) 217–226.
- [6] H. Akhlaghi, E. Roohi, S. Stefanov, A new iterative wall heat flux specifying technique in DSMC for heating/cooling simulations of MEMS/NEMS, *Int J Therm Sci* 59 (2012) 111–125.
- [7] H. Akhlaghi, E. Roohi, A novel algorithm for implementing a specified wall heat flux in DSMC: application to micro/nano flows and hypersonic flows, *Comput Fluids* 127 (2016) 78–101.
- [8] E.Y. Moghadam, E. Roohi, J.A. Esfahani, Heat transfer and fluid characteristics of rarefied flow in thermal cavities, *Vacuum* 109 (2014) 333–340.
- [9] E. Roohi, DSMC simulations of nanoscale and microscale gas flow, *encyclopedia of Microfluidics and nanofluidics*, second ed., (2014).
- [10] H.F. Oztop, I. Dagtekin, Mixed convection in two-sided lid-driven differentially heated square cavity, *Int J heat mass Transf* 47 (8) (2004) 1761–1769.
- [11] S. Naris, D. Valougeorgis, The driven cavity flow over the whole range of the Knudsen number, *Phys Fluids* (1994-present) 17 (9) (2005) 097106.
- [12] D. Auld, Y.L. Lan, Simulation of lid-driven cavity flow by parallel DSMC method, 24th applied aerodynamics conference, san Francisco, California, 2006.
- [13] S. Mizzi, D.R. Emerson, S.K. Stefanov, R.W. Barber, J.M. Reese, Effects of rarefaction on cavity flow in the slip regime, *J Comput Theor Nanosci* 4 (4) (2007) 817–822.
- [14] D.A. Perumal, V. Krishna, G. Sarvesh, A.K. Dass, Numerical simulation of gaseous microflows by lattice Boltzmann method, *Int J Recent Trends Eng* 1 (5) (2009) 15–20.
- [15] B. John, X.J. Gu, D.R. Emerson, Investigation of heat and mass transfer in a lid-driven cavity under nonequilibrium flow conditions, *Numer Heat Transf Part B Fundam* 58 (5) (2010) 287–303.
- [16] B. John, X.J. Gu, D.R. Emerson, Effects of incomplete surface accommodation on non-equilibrium heat transfer in cavity flow: a parallel DSMC study, *Comput fluids* 45 (1) (2011) 197–201.
- [17] A. Mohammadzadeh, E. Roohi, H. Niazmand, S. Stefanov, R.S. Myong, Thermal and second-law analysis of a micro-or nanocavity using direct-simulation Monte Carlo, *Phys Rev E* 85 (5) (2012) 056310.
- [18] A. Mohammadzadeh, E. Roohi, H. Niazmand, A parallel DSMC investigation of monatomic/diatomic gas flows in a micro/nano cavity, *Numer Heat Transf Part A Appl* 63 (4) (2013) 305–325.
- [19] A. Rana, M. Torrilhon, H. Struchtrup, Heat transfer in micro devices packaged in partial vacuum, *Journal of physics: conference series* (vol. 362, No. 1, p. 012034), IOP Publishing, 2012.
- [20] M. Vargas, G. Tatsios, D. Valougeorgis, S. Stefanov, Rarefied gas flow in a rectangular enclosure induced by non-isothermal walls, *Phys Fluids* 26 (5) (2014) 057101.
- [21] J.C. Huang, K. Xu, P. Yu, A unified gas-kinetic scheme for continuum and rarefied flows II: multi-dimensional cases, *Commun Comput Phys* 12 (3) (2012) 662–690.
- [22] R. Jyotsna, S.P. Vanka, Multigrid calculation of steady, viscous flow in a triangular cavity, *J Comput Phys* 122 (1) (1995) 107–117.
- [23] H.K. Moffatt, Viscous and resistive eddies near a sharp corner, *J Fluid Mech* 18 (1964) 1–18.
- [24] R.L. Panton, R.L. Panton (Ed.), *Incompressible flow*, fourth ed., Wiley Online Library, 2013.
- [25] A. Jagannathan, R. Mohan, M. Dhanak, A spectral method for the triangular cavity flow, *Comput Fluids* 95 (2014) 40–48.
- [26] E. Erturk, O. Gokcol, Fine grid numerical solutions of triangular cavity flow, *Eur Phys J Appl Phys* 38 (1) (2007) 97–105.
- [27] L.M. Gonzalez, M. Ahmed, J. Kuhn, H.C. Kuhlmann, V. Theofilis, Three-dimensional flow instability in a lid-driven isosceles triangular cavity, *J Fluid Mech* 675 (2011) 369–396.
- [28] M. Ahmed, H.C. Kuhlmann, Flow instability in triangular lid-driven cavities with wall motion away from a rectangular corner, *Fluid Dyn Res* 44 (2) (2012) 025501.
- [29] M.M. Rahman, R. Saidur, S. Mekhilef, M.B. Uddin, A. Ahsan, Double-diffusive buoyancy induced flow in a triangular cavity with corrugated bottom wall: effects of geometrical parameters, *Int Commun Heat Mass Transf* 45 (2013) 64–74.
- [30] Y. Sone, *Molecular gas dynamics: theory, techniques, and applications*, Springer Science & Business Media, 2007.
- [31] A. Rana, M. Torrilhon, H. Struchtrup, A robust numerical method for the R13 equations of rarefied gas dynamics: application to lid driven cavity, *J Comput Phys* 236 (2013) 169–186.
- [32] S.K. Stefanov, On DSMC calculations of rarefied gas flows with small number of particles in cells, *SIAM J Sci Comput* 33 (2011) 677–702.
- [33] B. Goshayeshi, E. Roohi, S. Stefanov, A novel Simplified Bernoulli Trials collision scheme in the DSMC with intelligence over particle distances, *Phys Fluids* 27 (10) (2015) 107104.
- [34] B. Goshayeshi, E. Roohi, S. Stefanov, DSMC simulation of hypersonic flows using an improved SBT-TAS technique, *J Comput Phys* 303 (C) (2015) 28–44.
- [35] A. Saadati, E. Roohi, Detailed investigation of flow and thermal field in micro/nano nozzle using simplified bernoulli trial (SBT) collision scheme in DSMC, *Aerosp Sci Technol* 46 (2015) 236–255.
- [36] E. Taheri, E. Roohi, S. Stefanov, On the convergence of the simplified Bernoulli trial collision scheme in rarefied Fourier flow, *Phys Fluids* 29 (6) (2017).
- [37] E. Roohi, S. Stefanov, A. Shoja-Sani, H. Ejraei, A generalized form of the Bernoulli trial collision scheme in DSMC: derivation and evaluation, *J Comp Phys* 354C (2018) 476–492.
- [38] E. Roohi, S. Stefanov, Collision Partner Selection Schemes in DSMC: from micro/nano flows to hypersonic flows, *Phys Rep* 656 (C) (2016) 1–38.
- [39] T.J. Scanlon, E. Roohi, C. White, M. Darbandi, J.M. Reese, An open source, parallel DSMC code for rarefied gas flows in arbitrary geometries, *Comput Fluids* 39 (10) (2010) 2078–2089.
- [40] C. White, M.K. Borg, T.J. Scanlon, J.M. Reese, A DSMC investigation of gas flows in micro-channels with bends, *Comput Fluids* 71 (2013) 261–271.
- [41] R.C. Palharini, C. White, T.J. Scanlon, R.E. Brown, M.K. Borg, J.M. Reese, Benchmark numerical simulations of rarefied non-reacting gas flows using an open-source DSMC code, *Comput Fluids* 120 (2015) 140–157.
- [42] V. Shahabi, T. Baier, E. Roohi, S. Hardt, On the radiometric flow between periodically structured nano-surfaces, *Sci Rep* 7 (41412) (2017) 1–14.
- [43] F.J. Alexander, A.L. Garcia, B.J. Alder, Cell size dependence of transport coefficients in stochastic particle algorithms, *Phys Fluids* (1994-present) 10 (6) (1998) 1540–1542.
- [44] N.G. Hadjiconstantinou, Analysis of discretization in the direct simulation Monte Carlo, *Phys Fluids* (1994-present) 12 (10) (2000) 2634–2638.
- [45] E. Roohi, M. Darbandi, Extending the Navier–Stokes solutions to transition regime

- in two-dimensional micro- and nanochannel flows using information preservation scheme, *Phys Fluids* 21 (2009) 82001.
- [46] C. Shu, X.H. Mao, Y.T. Chew, Particle number per cell and scaling factor effect on accuracy of DSMC simulation of micro flows, *Int J Numer Methods Heat Fluid Flow* 15 (8) (2005) 827–841.
- [47] O. Ejtehadi, E. Roohi, J.A. Esfahani, Investigation of basic molecular gas structural effects on hydrodynamics and thermal behaviors of rarefied shear driven micro/nano flow using DSMC, *Int Commun Heat Mass Transf* 39 (3) (2012) 439–448.
- [48] P.N. Shankar, M.D. Deshpande, Fluid mechanics in the driven cavity, *Annu Rev Fluid Mech* 32 (1) (2000) 93–136.
- [49] B. Rahimi, H. Struchtrup, Macroscopic and kinetic modelling of rarefied polyatomic gases, *J Fluid Mech* 806 (2016) 437–505.
- [50] A.M. Mahdavi, E. Roohi, Investigation of cold-to-hot transfer and thermal separation zone through nano step geometries, *Phys Fluids* 27 (7) (2015) 051507.
- [51] N.G. Hadjiconstantinou, A.L. Garcia, M.Z. Bazant, G. He, Statistical error in particle simulations of hydrodynamic phenomena, *J Comput Phys* 187 (1) (2003) 274–297.